

CORRESPONDENCE

Open Access

VH-CH1 switch region-inserting multispecific antibody designs and their efficacy against SARS-CoV-2 in vitro and in vivo

Lili Wu¹, Yue Gao^{1,2}, Dandan Yu^{3,4}, Sheng Liu⁵, Runchu Zhao¹, Dezhi Liu^{1,6}, Ling Xu^{3,4}, Honghui Liu¹, Xiaoyun Wang¹, Jianxun Qi¹, Yan Chai¹, Liya Wei², Yong-Gang Yao^{3,4,7,8}✉, George F. Gao^{1,7,9}✉ and Qihui Wang^{1,2,6,7}✉

Dear Editor,

To combat SARS-CoV-2 infection, numerous monoclonal antibodies have been developed. However, the virus's continuous variation has rendered most antibodies ineffective^{1,2}. Although there are broad-spectrum antibodies targeting conserved epitopes on the spike (S) proteins, their neutralizing potency is generally moderate^{1–3}, constraining further development. Rational design of multispecific antibodies could enhance the potency compared to parental counterparts⁴. Several strategies have been explored to counter SARS-CoV-2, like the IgG-scFv format of bsAb15⁵ and linker-connected bn03⁶, but their configurations are artificially engineered. Here, utilizing the natural VH-CH1 switch region-inserting scaffold found in malaria-exposed individuals⁷, we designed multiple bispecific (bsAbs) and trispecific (tsAbs) antibodies by combining the antibodies recognizing conserved epitopes on SARS-CoV-2 S but exhibiting moderate effectiveness.


Initially, by screening a previous nanobody library⁸, we identified a SARS-CoV-2 receptor-binding domain (RBD)-targeting nanobody R211. Binding assays revealed that R211 potently bound to all tested RBDs from SARS-CoV-2 and its variants, but its activities decreased in binding Omicron sub-variants (Supplementary Fig. S1). Pseudovirus-based neutralization results indicated that R211 showed broad but moderate potency against SARS-CoV-2 variants with half-maximal inhibitory concentration (IC₅₀) values around 0.1 µg/mL, and the activity further

decreased when neutralizing Omicron sub-variants (Supplementary Fig. S2). Flow cytometry-based assays further indicated that R211 can broadly bind to all tested sarbecovirus S proteins, though its ability was lower than our previously identified broad-spectrum antibodies IMCAS74 (namely 74) and S102 (Supplementary Fig. S3). Competition-binding assays indicated that, among the antibodies targeting eight epitope classes on RBD², R211 could compete with ADI-56046 (RBD-3), C022 (RBD-6) and H014 (RBD-7) (Supplementary Fig. S4), suggesting that R211 likely recognizes a cryptic epitope. Cryo-EM structure of R211 and SARS-CoV-2 S further revealed that R211 recognized the RBD-7 epitope (Supplementary Figs. S5, S6 and Table S1), and the binding sites were highly conserved among sarbecoviruses (Supplementary Fig. S6d). Detailed analysis indicated that S371L/F mutation in Omicron may break the hydrogen-bond interaction with R211 (Supplementary Fig. S6c), thereby weakening the binding.

Based on the broad breadth but moderate efficacy of R211 and three previous antibodies (74, S102 and R14), we supposed that combining these nonoverlapping antibodies may improve the neutralizing potency against SARS-CoV-2 variants (Fig. 1a). 74 recognizes a conserved epitope on the RBD as S2H97⁹, showing resistance to escape by SARS-CoV-2 variants². S102 targets the conserved stem-helix region of the S2 and exhibits pan-sarbecovirus neutralization³. R14 recognizes the receptor-binding motif and displays varied neutralization against SARS-CoV-2 variants⁸. Particularly, R211, S102 and R14 are nanobodies, which are easily manipulated. Therefore, we utilized the natural VH-CH1-inserting antibody format to design bsAbs by inserting nanobodies into the switch region between VH and CH1 of 74⁷, resulting in three bsAbs (R211-74, S102-74 and R14-74) (Fig. 1b). Simultaneously, we also designed

Correspondence: Yong-Gang Yao (yaoyg@mail.kiz.ac.cn) or George F. Gao (gaof@im.ac.cn) or Qihui Wang (wangqihui@im.ac.cn)
¹CAS Key Laboratory of Pathogen Microbiology and Immunology, Institute of Microbiology, Chinese Academy of Sciences, Beijing, China
²College of Life Science, Hebei University, Baoding, Hebei, China
Full list of author information is available at the end of the article
These authors contributed equally: Lili Wu, Yue Gao, Dandan Yu, Sheng Liu

© The Author(s) 2023

 **Open Access** This article is licensed under a Creative Commons Attribution 4.0 International License, which permits use, sharing, adaptation, distribution and reproduction in any medium or format, as long as you give appropriate credit to the original author(s) and the source, provide a link to the Creative Commons license, and indicate if changes were made. The images or other third party material in this article are included in the article's Creative Commons license, unless indicated otherwise in a credit line to the material. If material is not included in the article's Creative Commons license and your intended use is not permitted by statutory regulation or exceeds the permitted use, you will need to obtain permission directly from the copyright holder. To view a copy of this license, visit <http://creativecommons.org/licenses/by/4.0/>.

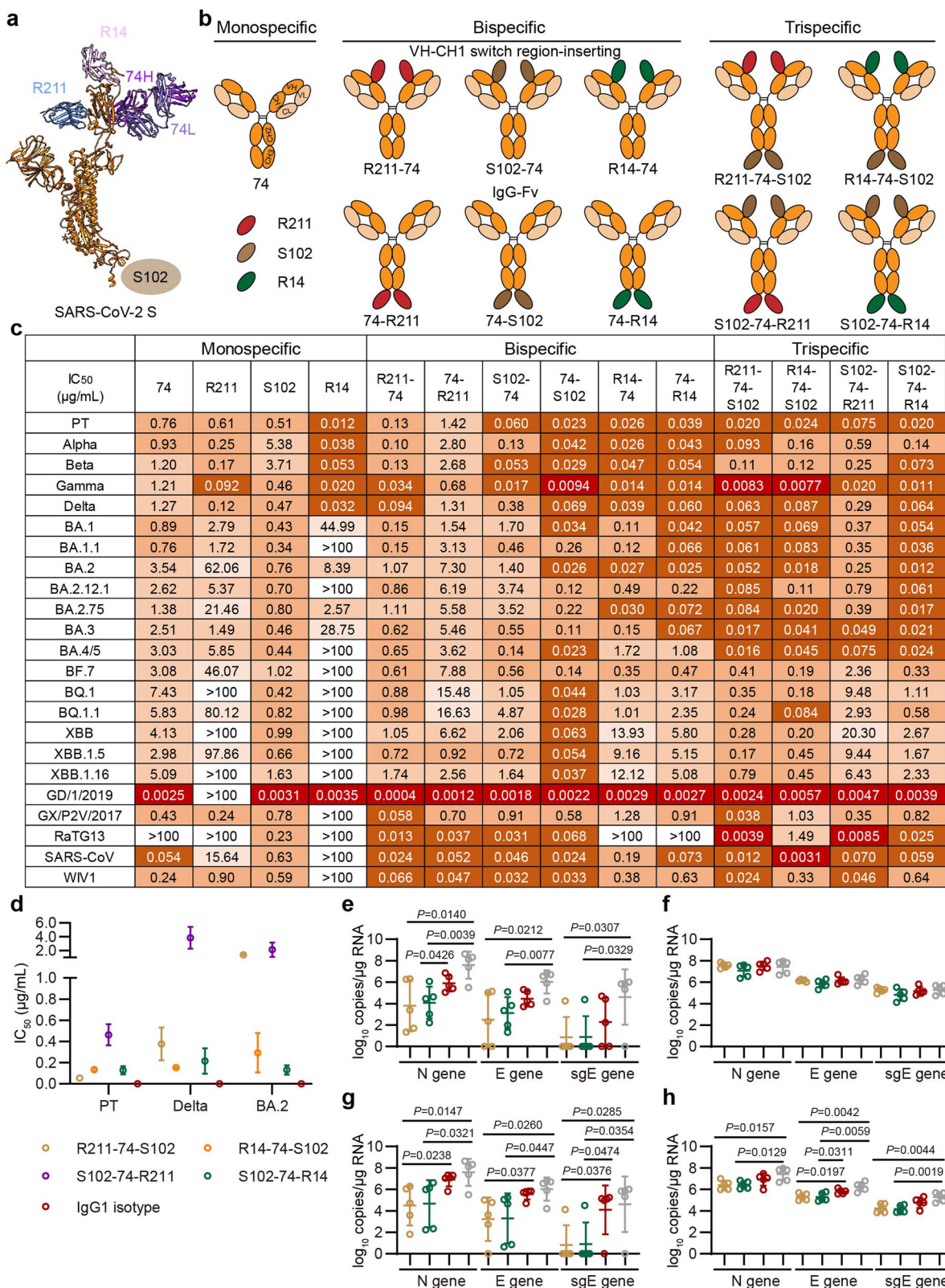


Fig. 1 (See legend on next page.)

(see figure on previous page)

Fig. 1 Design and efficacy of multispecific antibodies. **a** Epitopes of R211, 74, R14 and S102 on SARS-CoV-2 S protein with S102 shown schematically due to its unrevealed structure. **b** Schematic representation of designed multispecific antibodies. **c** Neutralization of multispecific antibodies against pseudotyped SARS-CoV-2 and other sarbecoviruses. The assay was independently repeated twice with two replicates ($n = 2$). Mean IC_{50} s from two independent experiments are shown. PT, SARS-CoV-2 prototype strain. **d** Neutralization of trispecific antibodies against live SARS-CoV-2 PT, Delta and BA.2. The assay was repeated twice with at least four replicates ($n \geq 4$). Mean IC_{50} s from two independent experiments are shown, with different antibodies represented by indicated circles. **e, f** Syrian hamsters ($n = 5$ per group) were prophylactically treated intraperitoneally (i.p.) with indicated antibody or PBS 6 h before intranasal (i.n.) challenge with BA.2. Viral titers of the N, E and subgenomic E (sgE) genes in lung (**e**) and nasal turbinate (**f**) 3 days post-infection (dpi) were detected. Antibodies are represented by different circles as in **d**, with gray circle indicating PBS. **g, h** Syrian hamsters ($n = 5$ per group) were therapeutically treated i.p. with the indicated antibody or PBS 6 h after i.n. challenge with BA.2. Viral titers of the N, E and sgE genes in lung (**g**) and nasal turbinate (**h**) 3dpi were detected. Antibodies are represented by different circles as in **e**. The P values in **e–h** were analyzed using unpaired two-tailed t -test.

three other bsAbs (74-R211, 74-S102 and 74-R14) for comparison based on the IgG-Fv format by fusing nanobodies to the CH3 of 74 (Fig. 1b).

Size-exclusion chromatography and SDS-PAGE profiles indicated that both formats of bsAbs can assemble correctly, exemplified by S102-74 and 74-S102 (Supplementary Fig. S7). To evaluate the efficacy of these bsAbs, we performed pseudovirus-based neutralization assays (Fig. 1c; Supplementary Fig. S8). We first evaluated their potency against SARS-CoV-2 prototype (PT) and the variants until BA.4/5. Regarding the VH-CH1-inserting format, compared to 74, R211-74 showed 3.0–35.9-fold increase against SARS-CoV-2 variants except BA.2.75; S102-74 exhibited 2.5–71.4-fold enhancement against Alpha, Beta, Gamma, Delta, BA.2, BA.3 and BA.4/5 and similar potency against other variants; and R14-74 displayed 5.3–130.1-fold enhancement against SARS-CoV-2 variants before BA.4/5 and slight increase against BA.4/5. While regarding the IgG-Fv format, 74-R211 showed similar or slightly decreased neutralization against SARS-CoV-2 variants compared to 74 and was lower than R211-74; 74-S102 displayed 2.9–135.4-fold enhancement against SARS-CoV-2 variants compared to 74 and was higher than S102-74; and 74-R14 showed similar potency to R14-74 and both were higher than 74. Notably, among these six bsAbs, 74-S102 showed the strongest potency against BA.4/5 (Fig. 1c).

Based on the effectiveness of these two bispecific formats, namely 74-S102 and S102-74, we further inserted R211 or R14 into either bsAb to design tsAbs, including R211-74-S102, R14-74-S102, S102-74-R211 and S102-74-R14 (Fig. 1b). The four tsAbs also assembled correctly, exemplified by R14-74-S102 and S102-74-R14 (Supplementary Fig. S7). Neutralization assays indicated that compared to 74-S102, R211-74-S102 and R14-74-S102 exhibited slightly increased or similar potency against SARS-CoV-2 variants including BA.4/5 (Fig. 1c; Supplementary Fig. S8). S102-74-R211 was weaker than R211-74-S102 but 4.2–112.1-fold better than 74-R211 against SARS-CoV-2 variants. S102-74-R14 was similar to R14-74-S102 and displayed comparable or slightly enhanced ability against SARS-CoV-2 variants compared to 74-R14.

Because of the potent neutralizing activities of tsAbs against pseudotyped SARS-CoV-2 variants, we also tested their potency against live SARS-CoV-2 virus. R211-74-S102, R14-74-S102 and S102-74-R14 showed good potencies against SARS-CoV-2 PT, Delta and BA.2, with IC_{50} values below 0.5 μ g/mL, except R211-74-S102 against BA.2 (Fig. 1d). R14-74-S102 and S102-74-R14 showed comparable activities against these viruses. In contrast, S102-74-R211 displayed weak neutralization against these viruses, consistent with the pseudovirus results (Fig. 1c). According to the in vitro potencies, we further selected R211-74-S102 and S102-74-R14 to assess their in vivo prophylactic and therapeutic activities (Fig. 1e–h). In the prophylactic groups, hamsters that received 15 mg/kg of R211-74-S102 or S102-74-R14 showed a significant 2–4-log reduced viral titers in the lung compared to the control groups (Fig. 1e). Notably, four of the five hamsters in both R211-74-S102 and S102-74-R14 groups exhibited undetectable subgenomic RNA of the E gene (sgE) in the lung. However, no significant improvement in viral titers in the nasal turbinate was observed (Fig. 1f). In the therapeutic groups, the two antibodies not only reduced viral titers in the lung (Fig. 1g) but also in the nasal turbinate (Fig. 1h). Consistent with the reduction of viral titers in the prophylactic groups, hamsters treated therapeutically with R211-74-S102 or S102-74-R14 exhibited undetectable sgE in the lungs of four of the five individuals. Overall, these results indicated that the two tsAbs can effectively prevent SARS-CoV-2 infections in the lungs when used prophylactically or therapeutically.

With the continuous evolution of Omicron, we assessed the neutralizing potency of the bsAbs and tsAbs against recent BF.7, BQ and XBB. Similarly, compared to 74, R211-74, S102-74 and 74-S102 still showed increased potency against these sub-variants, particularly 74-S102, which exhibited 55.0–205.5-fold enhancement against BQ and XBB with IC_{50} below 0.1 μ g/mL (Fig. 1c; Supplementary Fig. S8). 74-R211 showed similar or slightly decreased potency against these sub-variants compared to 74. However, although R14-74 and 74-R14 displayed enhanced activities against BF.7 and BQ, they showed decreased potency against XBB. S102-74-R14 showed enhanced potencies against BF.7, BQ and XBB compared to 74-R14.

S102-74-R211 showed increased potencies against BF.7 and BQ but decreased ability against XBB compared to 74-R211. Unexpectedly, compared to 74-S102, R211-74-S102 and R14-74-S102 exhibited decreased capabilities against BF.7, BQ and XBB. Additionally, we also assessed the efficacies of cocktail of 74, S102 and R211 and cocktail of 74, S102 and R14 against SARS-CoV-2 PT, Beta, BA.1, BA.2, BA.5 and XBB, which represent different serotypes according to our recently published data¹⁰. The results revealed that the efficacy of the cocktail of 74, R211 and S102 was generally weaker than that of S102-74-R211 and especially R211-74-S102 (Fig. 1c; Supplementary Fig. S9). Similarly, the efficacy of the cocktail of 74, R14 and S102 was also weaker than that of R14-74-S102 and S102-74-R14, but they were comparable when neutralizing PT and Beta, which may be due to the potent neutralization of R14.

Moreover, when neutralizing other sarbecoviruses, R211-74, 74-R211, S102-74 and 74-S102, especially R211-74, showed increased ability, whereas R14-74 and 74-R14 displayed comparable or slightly decreased activities, compared to 74 (Fig. 1c; Supplementary Fig. S8). Compared to 74-S102, R211-74-S102 showed enhanced potency, but R14-74-S102 displayed decreased activity. S102-74-R211 and S102-74-R14 exhibited similar or slightly increased abilities compared to 74-R211 and 74-R14, respectively. Notably, among these ten multispecific antibodies, R211-74-S102 displayed the highest potency against tested sarbecoviruses.

Antibody engineering plays a significant role in antibody therapy. Here, we explored a strategy mimicking the natural VH-CH1-inserting antibody identified in malaria-exposed individuals to design multispecific antibodies⁷, which exhibited significant enhancements against SARS-CoV-2 variants and other sarbecoviruses in vitro. In hamsters, tsAbs reduced viral titers in lung when used prophylactically or therapeutically. However, the difference observed in nasal turbinate between the prophylactic and therapeutic groups may be related to the limited antibody diffusion from circulation to nasal turbinate and the antibody pharmacokinetics. Our findings manifested the improved potency of these multispecific antibodies, suggesting potential antibody candidates against SARS-CoV-2 variants, as well as demonstrating the power of this natural scaffold for future antibody engineering.

Acknowledgements

We thank Dr. Zheng Fan, Dr. Xin Zhao, Dr. Pu Han (Institute of Microbiology, Chinese Academy of Sciences (CAS)), Dr. Yuanyuan Chen (Institute of Biophysics, CAS) and Dr. Xiao-Li Feng and Mrs. Ming-Hua Li (Kunming Institute of Zoology, CAS) for technical support. This work was supported by the National Key R&D Program of China (2022YFC2303403 and 2022YFC2604103), the CAS Project for Young Scientists in Basic Research (YSBR-010), and the National Natural Science Foundation of China (82225021 and 32070569).

Author details

¹CAS Key Laboratory of Pathogen Microbiology and Immunology, Institute of Microbiology, Chinese Academy of Sciences, Beijing, China. ²College of Life Science, Hebei University, Baoding, Hebei, China. ³Key Laboratory of Animal Models and Human Disease Mechanisms of the Chinese Academy of Sciences, and KIZ-CUHK Joint Laboratory of Bioresources and Molecular Research in Common Diseases, Kunming Institute of Zoology, Chinese Academy of Sciences, Kunming, Yunnan, China. ⁴Kunming National High-level Biosafety Research Center for Non-Human Primates, Center for Biosafety Mega-Science, Kunming Institute of Zoology, Chinese Academy of Sciences, Kunming, Yunnan, China. ⁵Cryo-EM Center, Department of Biology, Southern University of Science and Technology, Shenzhen, Guangdong, China. ⁶Institute of Physical Science and Information, Anhui University, Hefei, Anhui, China. ⁷University of the Chinese Academy of Sciences, Beijing, China. ⁸National Resource Center for Non-Human Primates, National Research Facility for Phenotypic & Genetic Analysis of Model Animals (Primate Facility), Kunming Institute of Zoology, Chinese Academy of Sciences, Kunming, Yunnan, China. ⁹Chinese Center for Disease Control and Prevention, Beijing, China

Author contributions

Q.W. and G.F.G. initiated and coordinated the project. Q.W. and L. Wu designed the experiments. Y.G., R.Z., and D.L. purified proteins and performed SPR assays. Y.G. performed pseudovirus-based neutralization and competition-binding assays. With the help of Y.G.Y., D.Y. and L.X. performed live virus assays. R.Z., X.W., and H.L. prepared SARS-CoV-2 S and R211 proteins for cryo-EM. S.L. and Y.C. collected cryo-EM data and solved the structure. L. Wu, Y.G., R.Z., D.Y., D.L., S.L., J.Q., L. Wei, Y.G.Y., Q.W., and G.F.G. analyzed the data. L. Wu, Y.G.Y., G.F.G., and Q.W. wrote the manuscript.

Data availability

Cryo-EM density map and atomic coordinates have been deposited in the Electron Microscopy Data Bank and Protein Data Bank under the codes EMD-36775 and 8K0N, respectively.

Conflict of interests

Q.W., G.F.G., L. Wu, R.Z., and J.Q. are coinventors of the patents for the multispecific antibodies in this study. The other authors declare no competing interests.

Publisher's note

Springer Nature remains neutral with regard to jurisdictional claims in published maps and institutional affiliations.

Supplementary information The online version contains supplementary material available at <https://doi.org/10.1038/s41421-023-00616-1>.

Received: 6 August 2023 Accepted: 17 October 2023

Published online: 11 November 2023

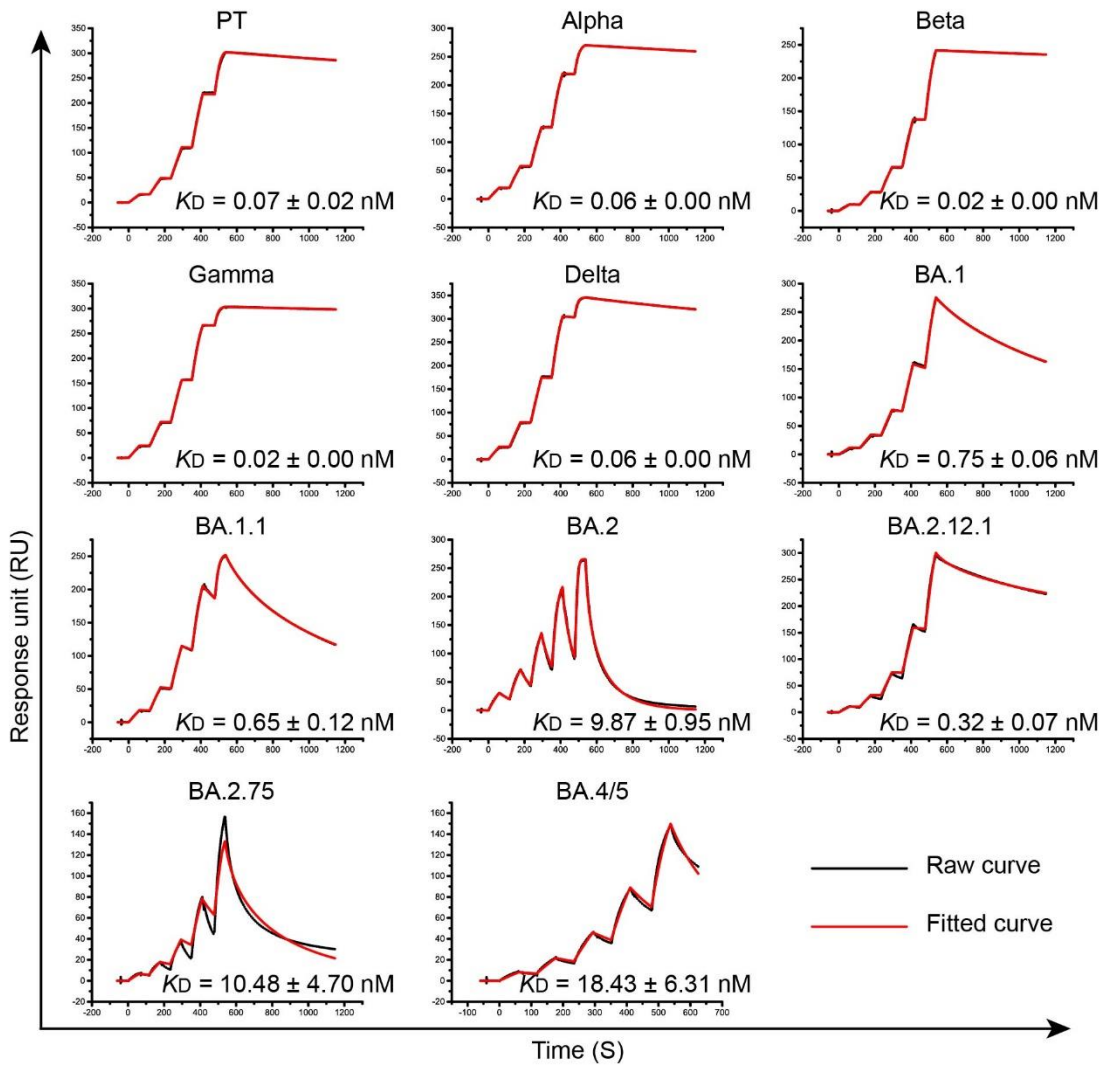
References

- Huang, M. et al. *Immunity* **55**, 1501–1514.e1503 (2022).
- He, Q. et al. *Cell Rep. Med.* **4**, 100991 (2023).
- Wang, X. et al. *Sci. Bull. (Beijing)* **68**, 684–687 (2023).
- Jin, S. et al. *Signal Transduct. Target. Ther.* **7**, 39 (2022).
- Li, Z. et al. *Nat. Immunol.* **23**, 423–430 (2022).
- Li, C. et al. *Cell* **185**, 1389–1401.e1318 (2022).
- Pieper, K. et al. *Nature* **548**, 597–601 (2017).
- Liu, H. et al. *Cell Rep. Med.* **4**, 100918 (2023).
- Starr, T. N. et al. *Nature* **597**, 97–102 (2021).
- Hu S. et al. *Sci. Bull. (in press)*.

Supplementary information

1
2
3

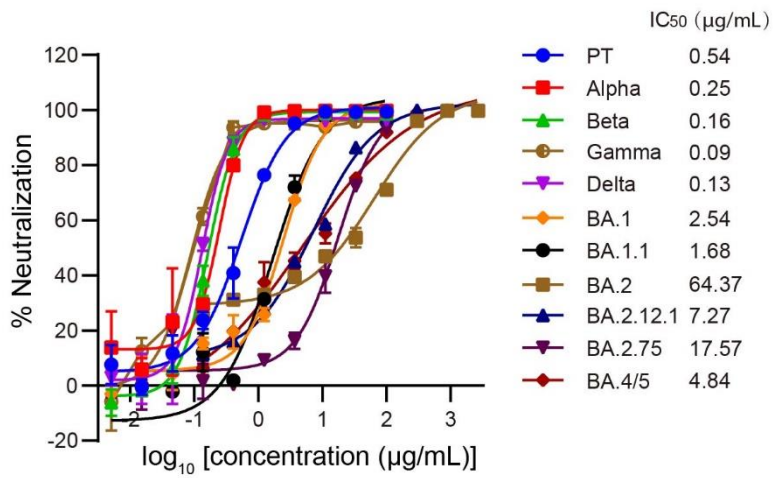
Fig. S1



4
5
6
7
8
9
10
11

Supplementary Fig. S1 Binding of R211 to RBDs from SARS-CoV-2 prototype (PT) and variants of concern (VOCs) tested by surface plasmon resonance (SPR) assays. The assay was repeated three times. The equilibrium dissociation constant (K_D) values were the mean \pm standard deviation (SD) of three independent experiments. The raw and fitted binding curves are shown as black and red lines, respectively. One representative run is shown of three independent experiments.

12 **Fig. S2**

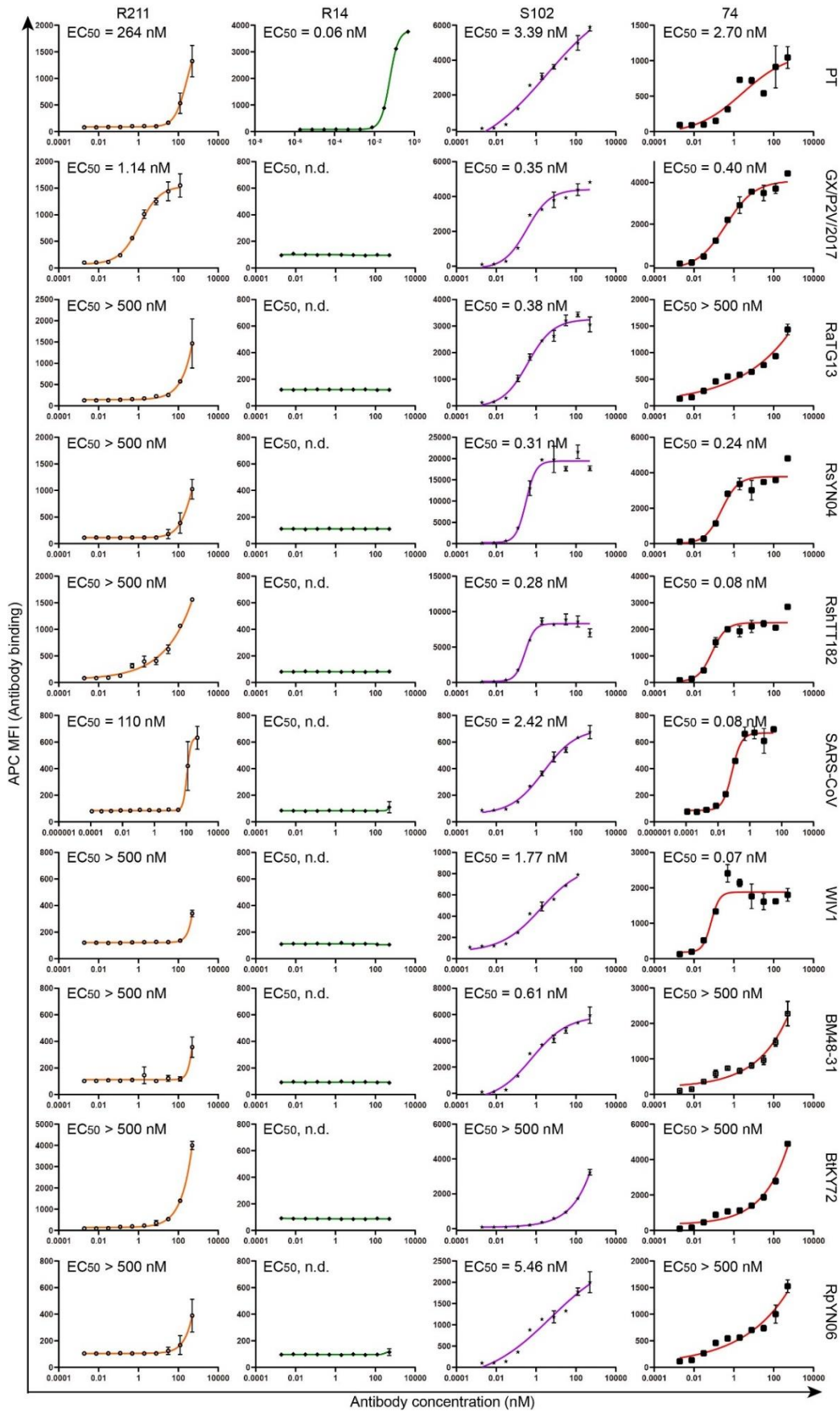


13

14 **Supplementary Fig. S2 Neutralizing activity of R211 against pseudotyped SARS-**
15 **CoV-2 PT and VOCs.** The assay was performed twice with two replicates ($n=2$) at
16 each time. Representative results of two independent experiments are shown.

17

18 Fig. S3

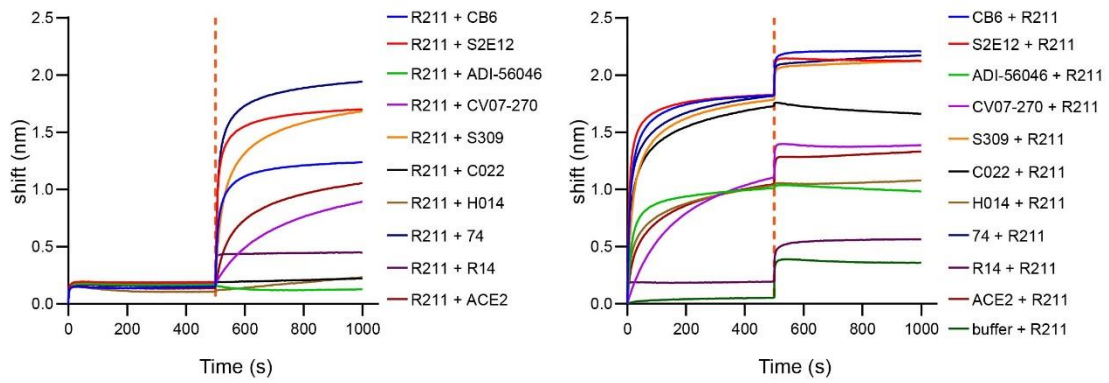


20 **Supplementary Fig. S3 Flow cytometry-based binding of R211, R14, S102 and 74**
21 **to spike (S) proteins of sarbecoviruses belonging to four clades.** SARS-CoV-2 PT,
22 GX/P2V/2017, RaTG13, RsYN04 and RsTTh182 belong to SARS-CoV-2 clade,
23 SARS-CoV and WIV1 belong to SARS-CoV clade, BM48-31 and BtKY72 belong to
24 Asia and Europe clade, and RpYN06 belongs to non-ACE2 binding clade. The assay
25 was repeated twice with two technical replicates ($n=2$) at each time. Representative
26 results of two independent experiments are shown. n.d, not determined.

27

28

29 **Fig. S4**

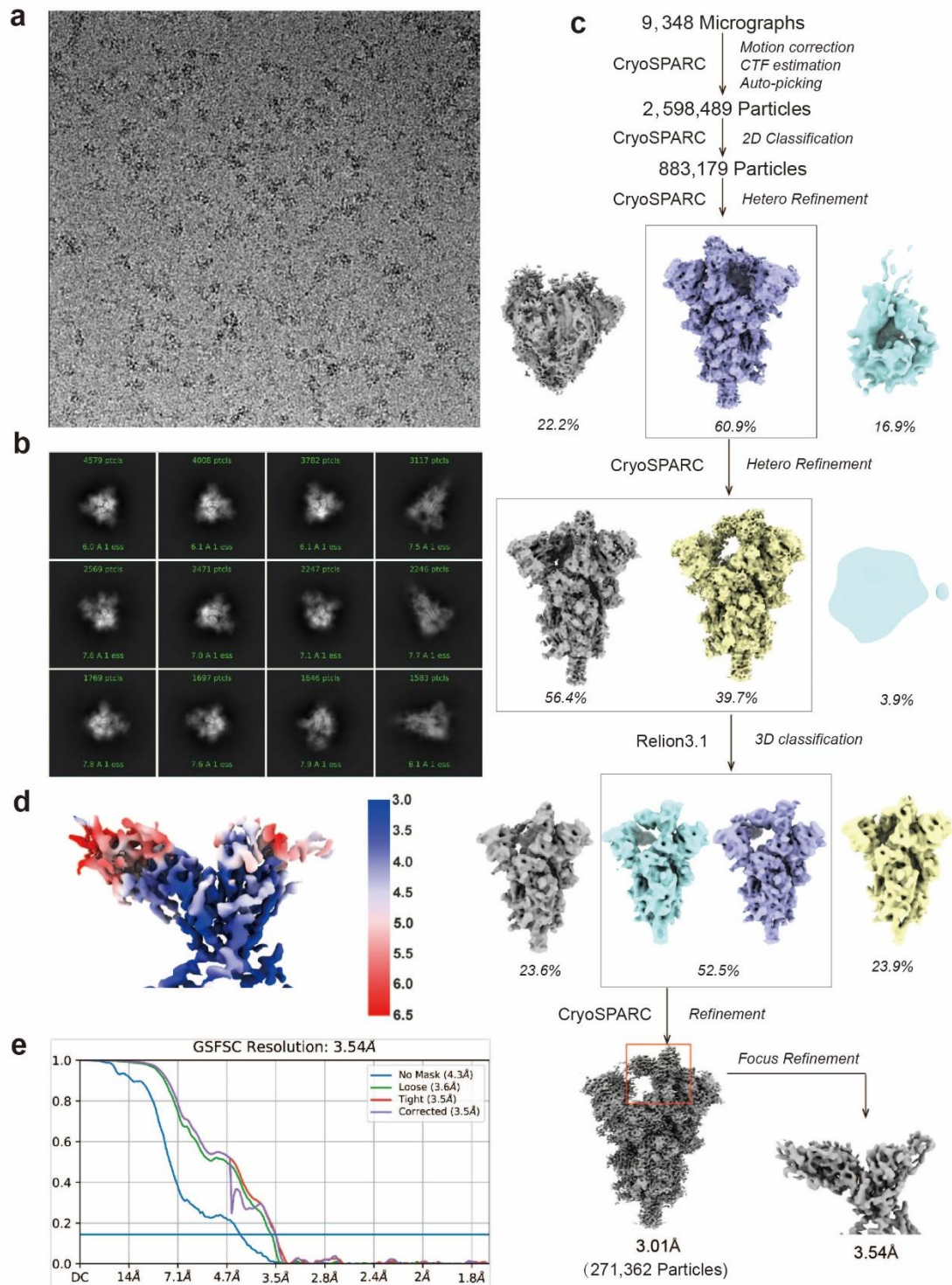


CB6 (RBD-1)	S2E12 (RBD-2)	ADI-56046 (RBD-3)	CV07-270 (RBD-4)
S309 (RBD-5)	C022 (RBD-6)	H014 (RBD-7)	74 (RBD-8)

30

31 **Supplementary Fig. S4 Competitive binding of R211 and monoclonal antibodies**
 32 **belonging to eight epitope classes on SARS-CoV-2 RBD, as measured by Octet**
 33 **RED96.** The assay was repeated twice. Shown data are one representative result.

34



36

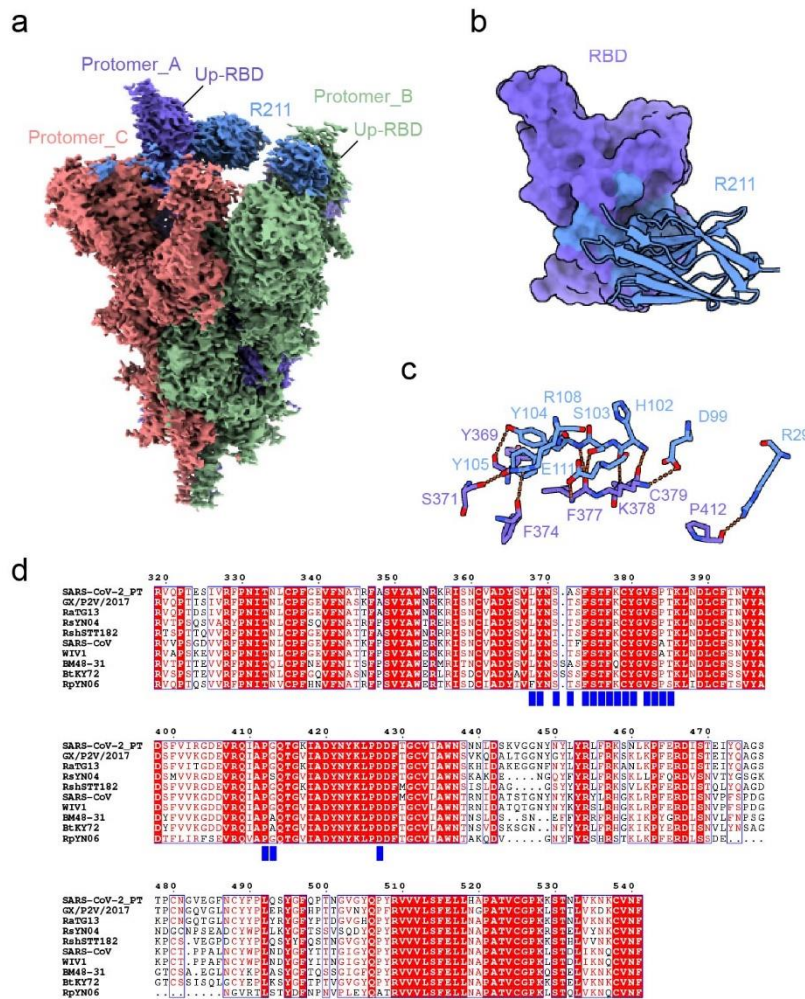
37 **Supplementary Fig. S5 Flow chart of single-particle analysis of the R211 in**
 38 **complex with SARS-CoV-2 S. a** Representative cryo-EM micrograph of the
 39 **R211/SARS-CoV-2 S. b** 2D class average images of the R211/SARS-CoV-2 S. **c** A brief

40 workflow of cryo-EM image processing and reconstruction. **d** Cryo-EM map of the
41 R211/SARS-CoV-2 S, colored by local resolution (Å). **e** The Fourier shell correlation
42 (FSC) curve for reconstruction.

43

44

45 **Fig. S6**



46

47 **Supplementary Fig. S6 Cryo-EM structure of R211 in complex with SARS-CoV-2**

48 **RBD.** **a** Cryo-EM map of R211 in complex with SARS-CoV-2 S at a 3.01 Å global

49 resolution. **b** The complex structure of R211 and SARS-CoV-2 RBD at 3.5 Å resolution

50 after local refinement. The footprint of R211 on RBD was displayed.

51 **c** Detailed interaction between R211 and RBD. Dashed lines represent hydrogen bonds or salt

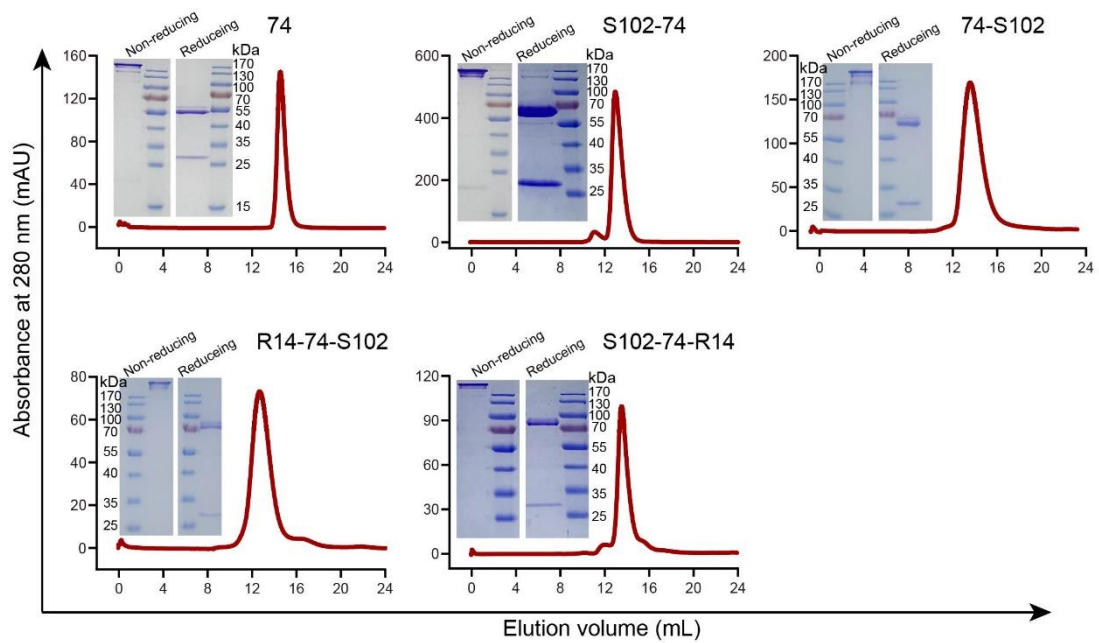
52 bridges. **d** The sequence conservation of the R211-binding epitope in the sarbecoviruses.

53 The binding sites of R211 on SARS-CoV-2 RBD were indicated in blue rectangles.

54

55

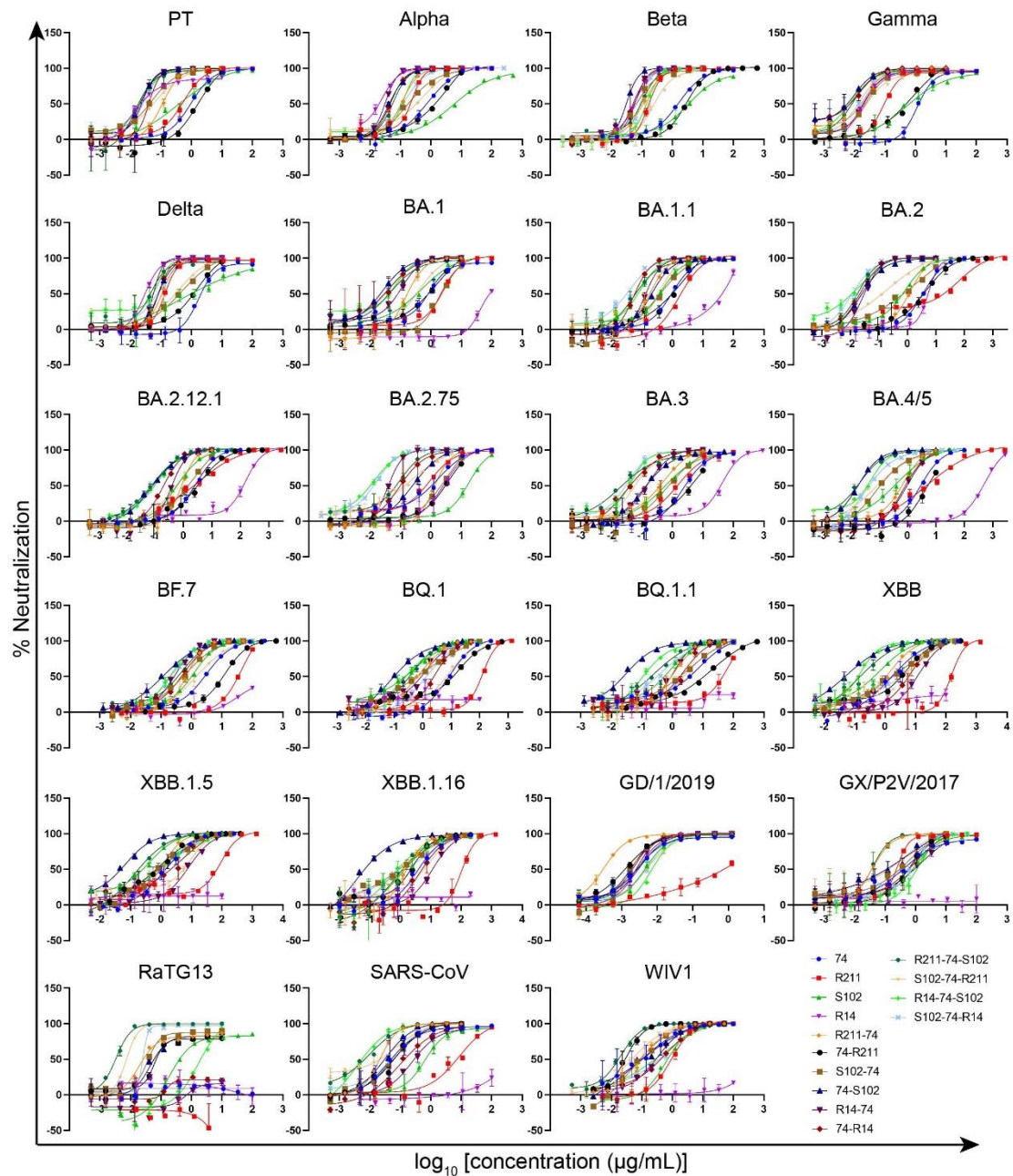
56 **Fig. S7**



57

58 **Supplementary Fig. S7 Size-exclusion chromatography analysis and SDS-PAGE**
59 **profiles (non-reducing and reducing) of multispecific antibodies.** The
60 chromatography analysis was measured using Superdex 200 Increase 10/300 GL
61 columns (GE Healthcare).

62



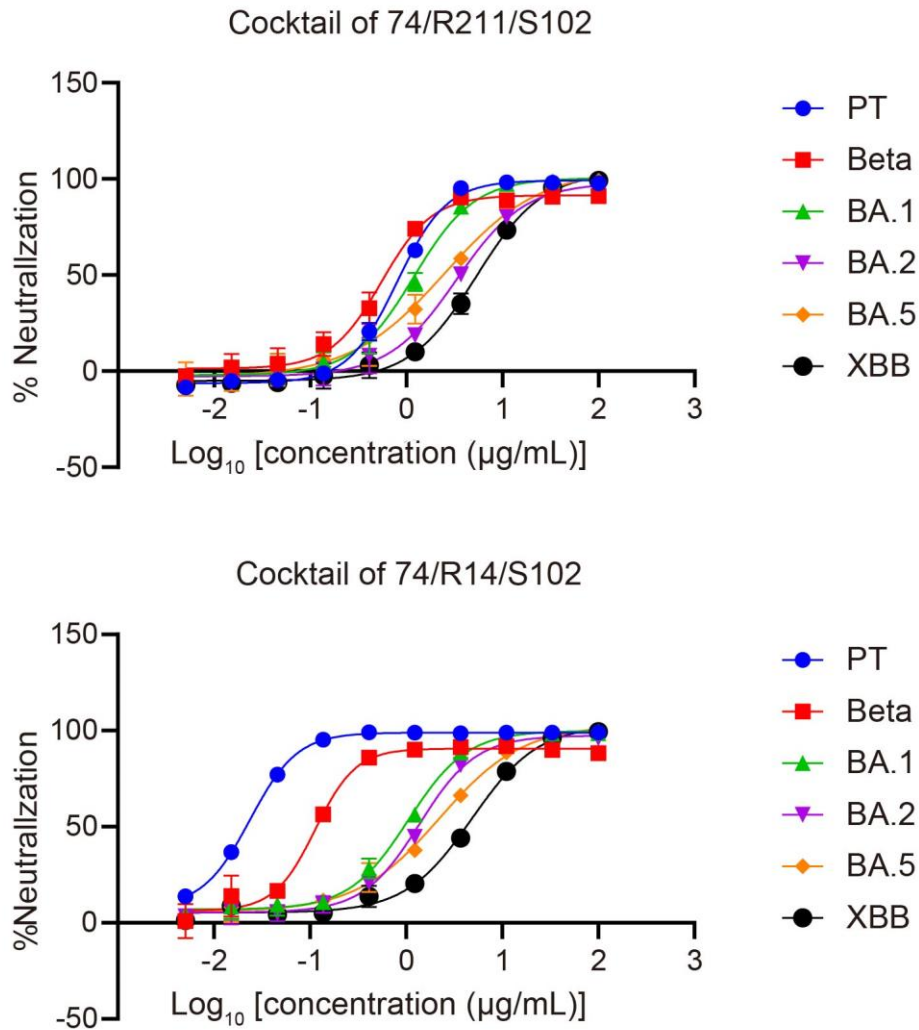
64

65 **Supplementary Fig. S8 Neutralization curves of 74, R211, S102, R14 and their**
 66 **multispecific antibodies against pseudotyped SARS-CoV-2 VOCs and other**
 67 **sarbecoviruses.** The neutralization curves shown here are one representative result of
 68 two independent experiments.

69

70

71 **Fig. S9**



IC ₅₀ (µg/mL)	PT	Beta	BA.1	BA.2	BA.5	XBB
cocktail of 74/R211/S102	0.81	0.56	1.17	3.29	2.38	5.16
cocktail of 74/R14/S102	0.026	0.10	1.05	1.37	2.30	4.86

72

73 **Supplementary Fig. S9 Neutralization of cocktail of 74, S102 and R211 or R14**

74 **against several pseudotyped SARS-CoV-2 VOCs.** The neutralization curves shown

75 here are one representative result of two independent experiments. The neutralizing

76 activities (IC₅₀) are the mean of two independent experiments.

77

78

79 **Supplementary Table S1 Cryo-EM data collection, refinement and validation**
 80 **statistics**

		R211/SARS-CoV-2 RBD
Data collection and processing		
Magnification		105k
Voltage (kV)		300
Electron exposure (e ⁻ /Å ²)		50
Defocus range (µm)		-1.2 to -2.2
Pixel size (Å)		0.84
Symmetry imposed		C1
Initial particle images (no.)		2,598,489
Final particle images (no.)		271,362
Map resolution (Å)		3.54
FSC threshold		0.143
Map resolution range (Å)		3.0-6.0
Refinement		
Initial model used (PDB code)		6M0J
Model resolution (Å)		3.54
Map sharpening <i>B</i> factor (Å ²)		-110.4
Model composition		
Non-hydrogen atoms		2513
Protein residues		317
Ligands		1
R.m.s. deviations		
Bond lengths (Å)		0.005
Bond angles (°)		0.982
Validation		
MolProbity score		1.96
Clashscore		8.60
Poor rotamers (%)		1.13
Ramachandran plot		
Favored (%)		95.53
Allowed (%)		4.47
Disallowed (%)		0.00

81

82

83 **Materials and methods**

84 **Cells, viruses and animals**

85 Vero E6 (ATCC, CRL-1586), HEK293T (ATCC, CRL-3216), BHK-21(ATCC, CCL-
86 10) and HEK293T-hACE2 (Genewiz[®]) were grown at 37 °C in Dulbecco's modified
87 Eagle's medium (DMEM) supplemented with 10% fetal bovine serum (FBS). Freestyle
88 293F cells were cultured in SMM 293-TII medium at 37 °C in a shaker with 5% CO₂.
89 The SARS-CoV-2 PT (Accession No. NMDCN0000HUI) was kindly provided by
90 Guangdong Provincial Center for Disease Control and Prevention (Guangdong, China).
91 The SARS-CoV-2 Delta (Accession No. NMDC60042793) and Omicron BA.2
92 (Accession No. NMDC60046377) strains were isolated in the Biosafety Level 3 (BSL3)
93 facility of Kunming Institute of Zoology, Chinese Academy of Sciences (CAS). All
94 virus strains were propagated by using the same protocol described in our previous
95 studies^{1,2}. Specific pathogen-free (SPF) male Syrian hamsters (3–4 weeks) were
96 purchased from Vital River (Beijing, China). All animal experiments in this study were
97 approved by the Institutional Animal Care and Use Committee (IACUC) at Kunming
98 Institute of Zoology, CAS. The animals used for SARS-CoV-2 challenge were
99 maintained at the Animal Biosafety Level 3 (ABSL3) facility.

100 **Protein expression and purification**

101 The coding sequences of SARS-CoV-2 RBDs (including PT, Alpha, Beta, Gamma,
102 Delta, Omicron sub-variants BA.1, BA.1.1, BA.2, BA.2.12.1, BA.2.75, BA.3 and
103 BA.4/5) and nanobodies R211, S102 and R14 with a C-terminal His-tag as well as R211
104 with a hFc-tag were cloned into the pCAGGS vector, respectively. The recombinant
105 plasmids were transfected into Freestyle 293F cells to express the RBD or nanobody
106 proteins, respectively. The heavy and light chain plasmids of 74 and multispecific
107 antibodies were cloned into the pCAGGS vector, respectively, and they were co-
108 transfected into Freestyle 293F cells at a ratio of 1:2 to express antibody proteins. After
109 5 days, the supernatants were collected, and His-tagged RBD and nanobody proteins
110 were purified by Ni affinity chromatography using a HisTrap excel 5 mL column (GE
111 Healthcare) and hFc-tagged antibodies were purified using a Protein A 5 mL column
112 (GE Healthcare). The proteins were further purified via gel filtration chromatography

113 with a Superdex 200 column (GE Healthcare).

114 **SPR analysis**

115 The binding affinities and kinetics between RBDs and R211 were analyzed using the
116 BIAcore 8K (GE Healthcare) at 25 °C in a single-cycle mode. PBST buffer (10 mM
117 Na₂HPO₄, 2 mM KH₂PO₄, 137 mM NaCl, 2.7 mM KCl, pH 7.4, and 0.005% (v/v)
118 Tween 20) was used as running buffer, and RBD proteins were changed into this buffer
119 by gel filtration before use. First, hFc-tagged R211 proteins were injected and captured
120 on a Protein A chip (GE Healthcare) at approximately 450 response units. Serially
121 diluted RBDs were then flowed over the surface of the chip to measure the binding
122 response. The dissociation time of R211 from SARS-CoV-2 PT, Alpha, Beta, Gamma,
123 Delta, BA.1, BA.1.1, BA.2, BA.2.12.1 and BA.2.75 RBDs was 600 s and from BA.4/5
124 RBD was 100 s. 10 mM Glycine-HCl (pH 1.5) was used to regenerate the chips. The
125 association constant (k_a), dissociation constant (k_d) and equilibrium dissociation
126 constant (K_D) of each pair of interactions were calculated using a 1:1 (Langmuir)
127 binding fit model with the BIAcore 8K evaluation software.

128 **Pseudovirus neutralization assay**

129 VSV-ΔG-GFP-based SARS-CoV-2 PT, Alpha, Beta, Gamma, Delta, BA.1, BA.1.1,
130 BA.2, BA.2.12.1, BA.2.75, BA.3, BA.4/5, BF.7, BQ.1, BQ.1.1, XBB, XBB.1.5,
131 XBB.1.6, GD/1/2019, GX/P2V/2017, RaTG13, SARS-CoV and WIV1 pseudoviruses
132 were prepared as previously described³. Briefly, 30 μg of the plasmids encoding viral
133 spike (S) protein with C-terminal 18 residues deleted (S-Δ18) was transfected into
134 HEK293T cells; 24 h later, the VSV-ΔG-G-GFP pseudoviruses were added there. After
135 1 h of incubation, the HEK293T cell culture medium was removed and replaced with
136 fresh DMEM containing 10 μg/mL of anti-VSV-G antibody (I1-Hybridoma ATCC®
137 CRL2700). After another 30 h, supernatants containing VSV-ΔG-GFP-based
138 pseudoviruses were harvested, centrifuged and filtered through a 0.45 μm sterilized
139 membrane filter. The pseudoviruses were then aliquoted and stored at -80 °C until use.
140 For the neutralization assay, Vero E6 cells were seeded in 96-well plates 12 h before
141 infection. Particularly, HEK293T-hACE2 cells were used for RaTG13 pseudovirus
142 infection. Antibodies were 3-fold serially diluted starting from 5400, 2700, 1200, 1000,

143 500, 200, 100, 50, 20, 10 or 2.5 µg/mL. Then, 50 µL of the serially diluted antibodies
144 were incubated with 50 µL of each pseudovirus at 1,000 transducing units at 37 °C for
145 1 h. The mixtures were then added to pre-prepared cells. After 15 h of incubation,
146 transducing unit numbers were calculated using a CQ1 confocal image cytometer
147 (Yokogawa). The results were analyzed using GraphPad Prism 8. Additionally, the
148 neutralizing potencies of 74, S102 and R211 cocktail and 74, S102 and R14 cocktail in
149 a molar ratio of 1:2:2 were also assessed against SARS-CoV-2 PT, Beta, BA.1, BA.2,
150 BA.4/5 and XBB.

151 **Flow cytometry assay**

152 The S-Δ18 of SARS-CoV-2 PT, GX/P2V/2017, RaTG13, RsYN04, RshTT182, SARS-
153 CoV, WIV1, BM48-31, BtKY72 or RpYN06 fused with green fluorescence protein
154 (GFP) at C-terminus were expressed on the cell surface by transfecting plasmids into
155 BHK-21 cells using PEI. After 6 h, the medium was changed to fresh DMEM
156 supplemented with 10% FBS. 48 h later, the cells were collected and transferred to a
157 96-well plate (2×10^5 cells/well) for staining. Briefly, 4-fold serially diluted His-tagged
158 R211, S102 and R14 and hFc-tagged 74 starting from 500 nM were incubated with the
159 cells at 37°C for 30 min, respectively, with the exception of R211 with GX/P2V/2017,
160 S102 with WIV1, R14 with SARS-CoV-2 PT and 74 with SARS-CoV, the starting
161 concentrations of which were 0.49 nM, 125 nM, 31.25 nM and 125 nM, respectively.
162 Subsequently, cells were washed twice and further stained with anti-His/APC antibody
163 (Miltenyi Biotec, AB_2751870) for R211, S102 and R14 and anti-hFc/APC antibody
164 (Biolegend, 409306) for 74 at 37°C for 30 min. After washing, the cells were analyzed
165 using BD LSRFortessa. The results were analyzed using FlowJo V10 and GraphPad
166 Prism 8.

167 **Epitope competition assay**

168 Epitope competition experiments were performed using an Octet RED96 instrument
169 (ForteBio) at 30°C with shaking at 1,000 rpm. Biotinylated SARS-CoV-2 PT RBD
170 proteins were immobilized on SA biosensors (Sartorius) at 15 µg/mL. The first antibody
171 was captured at 200 nM for 500 s and then 200 nM of the second antibody was

172 associated for 500 s in the presence of the first antibody. The bound antibodies were
173 finally removed with 10 mM Glycine (pH 2.5). The results were analyzed using
174 ForteBio Octet Data Analysis Software 9.0 and GraphPad Prism 8.

175 **Cryo-EM sample preparation and data acquisition**

176 For the R211/SARS-CoV-2 S complex, C-flat R2/1 (300 mesh) holey carbon grids were
177 first glow discharged for 20 s using a Pelco easiGlow glow discharge unit and 3 μ L
178 protein was applied to the surface of the grid at a temperature of 4°C and a humidity
179 level of 95%. Grids were then blotted for 2 s before being plunge-frozen in liquid ethane
180 using Vitrobot Mark IV (Thermo Fisher Scientific). Grids were imaged using 300 kV
181 Titan Krios electron microscope (Thermo Fisher Scientific) equipped with Falcon4
182 direct electron detector. The microscope is equipped with a GIF-Quantum energy filter
183 (Gatan), which was used with a slit width of 10 eV. Automatic data collection was
184 performed using EPU software. Images were recorded with Falcon4 direct electron
185 detector operating in counting mode at pixel size of 0.84 Å. The exposure was
186 performed with a dose rate of 15 e-/pixel/s and an accumulative dose of \sim 50 e-/Å² for
187 each image which was fractionated into 40 movie-frames. The final defocus ranges of
188 the datasets were approximately -(1.2-2.2) μ m.

189 **Image processing and 3D reconstruction**

190 A total of 9,348 super-resolution movies were collected and corrected for drift using
191 MotionCorr2⁴, and contrast transfer function (CTF) parameters were determined using
192 CTF estimation in patch mode⁵. Micrographs with an estimated resolution limit worse
193 than 5 Å were discarded in the initial screening. Blob particle picking, particle
194 extraction and 2D classification were performed on a subset of 1,000 micrographs.
195 Good classes were selected and subjected to template picking, which results in a total
196 of 2,598,489 particles. After extraction and split, these particles were used in batch 2D
197 classifications. A clean dataset with 883,179 particles from good 2D classes was
198 selected and subjected to two rounds initial reconstruction and heterogeneous
199 refinement. Two predominant classes showed the good structural features were

200 imported to Relion-3.1 for further 3D classification. After one round of 3D
201 classification, 271,362 particles were selected and imported back to cryoSPARC⁶ and
202 obtained the structure at a 3.01 Å global resolution. Local refinement focused on the
203 R211/SARS-CoV-2 RBD with mask could reconstitute complex structure at a 3.54 Å
204 resolution. Local resolution estimate was performed with cryoSPARC.

205 **Model building**

206 The structure of the SARS-CoV-2 RBD (PDB:6M0J), was docked into the cryo-EM
207 density maps of the R211/SARS-CoV-2 RBD complex of using CHIMERA⁷. The
208 model was manually corrected for local fit in COOT⁸ and the sequence register was
209 updated based on alignment. The model was refined against corresponding map in real
210 space using PHENIX⁹, in which the secondary structural restraints and Ramachandran
211 restrains were applied. The stereochemical quality of each model was assessed using
212 MolProbity¹⁰. Statistics for model refinement and validation are shown in Table S1.

213 **Live SARS-CoV-2 virus neutralization assay**

214 The neutralizing activities of antibodies against live SARS-CoV-2 virus were
215 determined based on the cytopathic effect (CPE). Briefly, 50 µL of 3-fold serial
216 dilutions (starting concentration 25 µg/mL) of antibodies were incubated with an equal
217 volume of 100 TCID₅₀ of live SARS-CoV-2 virus at 37°C for 1 h. The mixtures were
218 then added to Vero E6 cells (96-well plate, 2×10⁴ cells/well) and incubated for 4 days
219 at 37°C. CPE was observed and recorded on day 5. The results were analyzed using
220 GraphPad Prism 8. All experiments were performed in the BSL-3 facility of Kunming
221 Institute of Zoology, CAS.

222 **Animal protection experiments**

223 Three- to four-week-old male Syrian hamsters were purchased from Vital River
224 (Beijing, China) and randomly allocated to groups. All of the infected animals were
225 housed at the ABSL-3 facility of Kunming Institute of Zoology, CAS on a 12-h
226 light/dark cycle, with free access to food and water. In the prophylactic experiment, 15
227 mg/kg indicated antibodies or PBS were administered by intraperitoneal route (i.p.) 6

228 h before intranasal infection with 100 μ L of BA.2 at 1×10^4 TCID₅₀. In the therapeutic
229 experiment, animals were treated with 15 mg/kg indicated antibodies or PBS 6 h
230 following intranasal infection with BA.2 at the same dose. All hamsters were
231 euthanized three days post-infection, and lungs and nasal turbinates were collected for
232 the determination of viral titers. All experiments were performed at the ABSL3 facility
233 of Kunming Institute of Zoology, CAS.

234 **Measurement of viral RNAs**

235 The amounts of RNA copies per microgram RNA of lungs were determined using a
236 quantitative real-time PCR (qRT-PCR) assay as described in our previous study¹¹. In
237 brief, Trizol Reagent (Thermo Fisher Scientific, USA) was used for homogenized tissue
238 RNA isolation. Isolated RNAs were detected by one-step RT-PCR using a
239 THUNDERBIRD Probe One-Step qRT-PCR kit (TOYOBO, Japan) and amplified in a
240 BioRad CFX Real-Time PCR system. The PCR conditions were 10 min at 50 °C for
241 reverse transcription, 60 s at 95 °C, followed by 40 cycles of 95 °C for 15 s and 60 °C
242 for 45 s. We used the following forward (F) and reverse (R) primers and probe (P) for
243 quantification of viral copies: genomic N gene, N-F 5'-
244 GGGGAACTTCTCCTGCTAGAAT-3'/N-R 5'-CAGACATTTTGCTCTCAAGCTG-
245 3', probe N-P 5'-FAM-TTGCTGCTGCTTGACAGATT-TRMRA-3'; genomic E gene,
246 E-F 5'-ACAGGTACGTTAATAGTTAATAGCGT-3'/E-R 5'-
247 ATATTGCAGCAGTACGCACACA-3', probe E-P 5'-FAM-
248 AACTAGCCATCCTTACTGCGCTTCG-TRMRA-3'; subgenomic E gene (sgE),
249 sgE-F 5'-CGATCTCTTGTAGATCTGTTCTC-3'/sgE-R 5'-
250 ATATTGCAGCAGTACGCACACA-3', probe sgE-P 5'-FAM-
251 AACTAGCCATCCTTACTGCGCTTCG-TAMRA-3'. In each run, serial dilutions of
252 the SARS-CoV-2 RNA reference standard (National Institute of Metrology, China)
253 were used in parallel to calculate copy numbers in each sample.

254

255 **References**

- 256 1 Xu, L. *et al.* COVID-19-like symptoms observed in Chinese tree shrews infected with SARS-
257 CoV-2. *Zool. Res.* **41**, 517-526 (2020).
- 258 2 Feng, X. L. *et al.* Characteristics of replication and pathogenicity of SARS-CoV-2 Alpha and

259 Delta isolates. *Viol. Sin.* **37**, 804-812 (2022).
260 3 Zheng, A. *et al.* A binding-enhanced but enzymatic activity-eliminated human ACE2 efficiently
261 neutralizes SARS-CoV-2 variants. *Signal Transduct Target Ther* **7**, 10 (2022).
262 4 Zheng, S. Q. *et al.* MotionCor2: anisotropic correction of beam-induced motion for improved
263 cryo-electron microscopy. *Nat. Methods* **14**, 331-332 (2017).
264 5 Rohou, A. & Grigorieff, N. CTFFIND4: Fast and accurate defocus estimation from electron
265 micrographs. *J Struct Biol* **192**, 216-221 (2015).
266 6 Punjani, A., Rubinstein, J. L., Fleet, D. J. & Brubaker, M. A. cryoSPARC: algorithms for rapid
267 unsupervised cryo-EM structure determination. *Nat. Methods* **14**, 290-296 (2017).
268 7 Pettersen, E. F. *et al.* UCSF Chimera--a visualization system for exploratory research and
269 analysis. *J. Comput. Chem.* **25**, 1605-1612 (2004).
270 8 Emsley, P. & Cowtan, K. Coot: model-building tools for molecular graphics. *Acta Crystallogr.*
271 *D Biol. Crystallogr.* **60**, 2126-2132 (2004).
272 9 Adams, P. D. *et al.* PHENIX: a comprehensive Python-based system for macromolecular
273 structure solution. *Acta Crystallogr. D Biol. Crystallogr.* **66**, 213-221 (2010).
274 10 Chen, V. B. *et al.* MolProbity: all-atom structure validation for macromolecular crystallography.
275 *Acta Crystallogr. D Biol. Crystallogr.* **66**, 12-21 (2010).
276 11 Yu, D. *et al.* Infectivity of SARS-CoV-2 and protection against reinfection in rats. *Zool. Res.* **43**,
277 945-948 (2022).
278